

Numerical investigation of 3D effects on a 2D-dominated shocked mixing layer

Daniel Reese and Christopher Weber

Citation: *Physics of Fluids* **28**, 114102 (2016); doi: 10.1063/1.4966683

View online: <http://dx.doi.org/10.1063/1.4966683>

View Table of Contents: <http://scitation.aip.org/content/aip/journal/pof2/28/11?ver=pdfcov>

Published by the [AIP Publishing](#)

Articles you may be interested in

[The effect of mix on capsule yields as a function of shell thickness and gas fill](#)

Phys. Plasmas **21**, 062703 (2014); 10.1063/1.4882247

[On the evolution of spherical gas interfaces accelerated by a planar shock wave](#)

Phys. Fluids **23**, 084104 (2011); 10.1063/1.3623272

[Investigation of Rayleigh–Taylor turbulence and mixing using direct numerical simulation with experimentally measured initial conditions. II. Dynamics of transitional flow and mixing statistics](#)

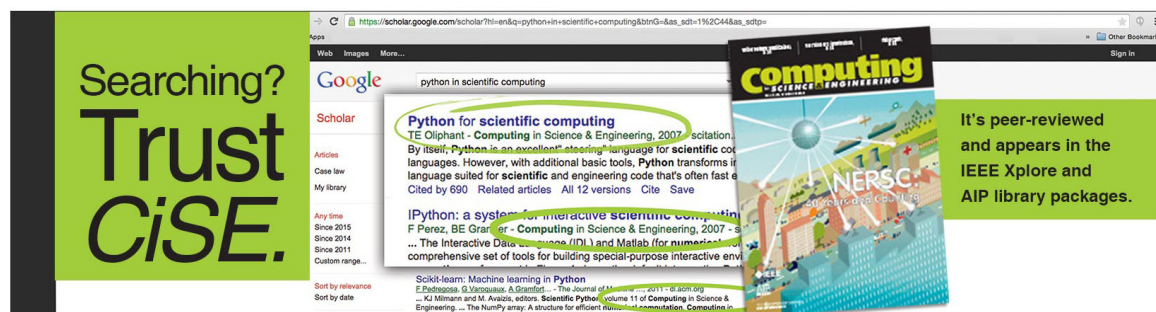
Phys. Fluids **21**, 014107 (2009); 10.1063/1.3064121

[Shock gaseous cylinder interactions: Dynamically validated initial conditions provide excellent agreement between experiments and numerical simulations to late–intermediate time](#)

Phys. Fluids **16**, 1203 (2004); 10.1063/1.1651483

[Direct numerical simulation and subgrid analysis of a transitional droplet laden mixing layer](#)

Phys. Fluids **12**, 650 (2000); 10.1063/1.870271

A composite image featuring a 'Trust CiSE' banner on the left, a Google Scholar search result for 'python in scientific computing' in the center, and a book cover for 'Computing in Science & Engineering' on the right. The banner has the text 'Searching? Trust CiSE.' in white on a green background. The search result shows the title 'Python for scientific computing' by J. E. Oliphant, published in 2007, with a snippet of text describing Python's use in scientific computing. The book cover is colorful and features the text 'Computing in Science & Engineering' and 'NERSC 20 years and counting'.

Numerical investigation of 3D effects on a 2D-dominated shocked mixing layer

Daniel Reese^{1,2,a)} and Christopher Weber²

¹University of Wisconsin, Madison, Wisconsin 53706, USA

²Lawrence Livermore National Laboratory, Livermore, California 94550, USA

(Received 1 June 2016; accepted 18 October 2016; published online 3 November 2016)

A nominally two-dimensional interface, unstable to the Rayleigh-Taylor or Richtmyer-Meshkov instability, will become three-dimensional at high Reynolds numbers due to the growth of background noise and 3D effects like vortex stretching. This three-dimensionality changes macroscopic features, such as the perturbation growth rate and mixing, as it enhances turbulent dissipation. In this study, a 2D perturbation with small-scale, 3D fluctuations is modeled using the hydrodynamics code *Miranda*. A Mach 1.95 shockwave accelerates a helium-over-SF₆ interface, similar to the experiments of Motl *et al.* [“Experimental validation of a Richtmyer-Meshkov scaling law over large density ratio and shock strength ranges,” *Phys. Fluids* **21**(12), 126102 (2009)], to explore the regime where a 2D dominated flow will experience 3D effects. We report on the structure, growth, and mixing of the post-shocked interface in 2D and 3D. *Published by AIP Publishing.* [<http://dx.doi.org/10.1063/1.4966683>]

I. INTRODUCTION

The interface between gases of two densities will become unstable when accelerated continuously in the direction of the density gradient, resulting in the Rayleigh-Taylor instability (RTI),^{1,2} or accelerated impulsively in any direction, resulting in the Richtmyer-Meshkov instability (RMI).^{3,4} These instabilities are governed by the vorticity transport equation,⁵

$$\frac{D\omega}{Dt} = (\omega \cdot \nabla) \mathbf{U} - \omega (\nabla \cdot \mathbf{U}) + \nu \nabla^2 \omega + \frac{1}{\rho^2} (\nabla \rho \times \nabla p), \quad (1)$$

where the non-zero cross product of the density and pressure gradients in the final term will lead to the production of vorticity. The first term on the right of Eq. (1) is the vortex stretching term, where a velocity gradient in the direction of the vorticity vector can lead to an amplification of vorticity and a reduction of its length scale. Eventually this effect can allow the third term on the right of Eq. (1) to dissipate the energy through viscous effects. Vortex stretching is fundamentally a three-dimensional effect and is responsible for the cascade of length scales in turbulent flows.⁶ Therefore dissipation and scalar mixing can be expected to increase in three-dimensional flows when compared with two-dimensional flows. Often the RMI and RTI are studied by imposing a well-defined, 2D, single mode perturbation. In experiments, higher mode, 3D perturbations are unavoidable and can eventually grow to break the two-dimensional nature of the interface.

In past numerical studies of shock tube experiments, three-dimensional features were necessary to match experimental results. The gas curtain shock tube experiments⁷ use a downward flowing layer of high-density SF₆ surrounded by air within a horizontal shock tube to study the shock-induced mixing. Previous work by Gowardhan and Grinstein⁸ simulated the LANL gas curtain experiments and found it necessary to add 3D noise to match post-reshock behavior. Schilling and Latini⁹ used a similar approach for the Vetter and Sturtevant experiments¹⁰ and observed that the late-time behavior was sensitive to the magnitude of the small-scale perturbations. Cabot¹¹

^{a)} Author to whom correspondence should be addressed. Electronic mail: dreese@wisc.edu

compared 2D vs 3D Rayleigh-Taylor with the same initial condition as the Cabot and Cook 3D direct numerical simulation (DNS),¹² while Olson and Greenough have done a similar 2D vs 3D comparison for the RMI.¹³ Both studies find that 3D effects reduce the large-scale extent of the mixing layer, but 3D flows develop more molecular mixing.

In some regimes, such as inertial confinement fusion and astrophysics, experiments are often modeled in two dimensions due to limited computational resources. In some cases,¹⁴ the simulations show clear nonlinearity; therefore, it is important to know at what point the 2D simulations diverge from 3D reality. Some high energy density physics (HEDP) experiments relevant to inertial confinement fusion (ICF)¹⁵ are initialized with 2D perturbations for simplicity, but at what point do 3D effects dominate?

This study takes a different approach from the previous computational studies. In this case, the problem is dominated by a two-dimensional flow and we investigate when and how 3D features break that two-dimensionality. The basis for this study is the shock tube experiments of Motl *et al.*¹⁶ These experiments used a nominally two-dimensional perturbation to study the Richtmyer-Meshkov instability but observed turbulent-like features at high Atwood and Mach numbers. The problem setup and a description of the code used for this study are given in Section II. Section III describes the differences in interface growth and mixing due to small-scale and 3D effects. Finally, concluding remarks are given in Section IV.

II. SIMULATION DETAILS

The single mode interface used here is based on experimental work¹⁶ which sets up a helium-over-SF₆ interface (Atwood number = 0.95) with an $\eta = 2.72$ cm amplitude and $\lambda = 16.7$ cm wavelength perturbation and accelerated it with a $M = 1.95$ shock wave. Experimental images were obtained by seeding a smoke tracer into the dense SF₆ gas and utilizing planar Mie scattering for imaging a 2D slice of the flow. In the current work, the interface characteristics and Mach number of the experiment are used and three dimensional effects are induced by adding small-scale perturbations using a Gaussian band of energy in wavenumber space described by

$$E(k) \propto e^{-\frac{(k-k_{peak})^2}{2\sigma^2}}, \quad (2)$$

where k is the magnitude of a wavevector in Fourier space, k_{peak} is the peak wavenumber, σ is the bandwidth, and

$$A_{RMS}^2 = \int_0^\infty E(k) dk. \quad (3)$$

Modes 3 through $2/3$ times the Nyquist cutoff ($nx/2$) are included in the creation of the small-scale perturbations, and the perturbation spectrum is zeroed outside of this range. RMS amplitude of $\frac{A_{RMS}}{\eta} = 0.03$ is used in both 2D and 3D and an additional case is included where these perturbations are reduced further, to $\frac{A_{RMS}}{\eta} = 0.003$. While the experiment certainly had small-scale 3D perturbations, their magnitude and scale are unknown (as is the sensitivity of simulations to these values) and the small-scale perturbations used in this study are purely postulated to investigate their effect. This initial condition is shown in Fig. 1, which shows (a) the single mode perturbation, (b) the

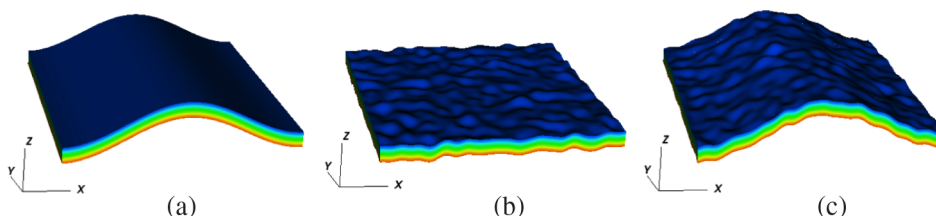


FIG. 1. Initial condition creation for the 3D case. (a) Single mode interface; (b) small-scale perturbations; (c) initial condition given by the superposition of (a) and (b).

TABLE I. Properties of each simulation. SM indicates a single-mode case, while MM indicates a multi-mode simulation.

Case	Mesh-size [x(y)×z]	Pert. [k_{peak} , σ , $\frac{A_{rms}}{\eta}$]	Single-mode pert. [λ , η , δ]
SM	256 × 1024	N/A	16.7 cm, 2.72 cm, 0.5143 cm
MM_2D	256 × 1024	$8 \frac{1}{cm}$, $4 \frac{1}{cm}$, 0.03	16.7 cm, 2.72 cm, 0.5143 cm
MM_3D	256 × 256 × 1024	$8 \frac{1}{cm}$, $4 \frac{1}{cm}$, 0.03	16.7 cm, 2.72 cm, 0.5143 cm
MM_3D_small	256 × 256 × 1024	$8 \frac{1}{cm}$, $4 \frac{1}{cm}$, 0.003	16.7 cm, 2.72 cm, 0.5143 cm

small scale $\frac{A_{RMS}}{\eta} = 0.03$ perturbations, and (c) the final interface. To simulate diffusion, the interface contains a hyperbolic tangent cross-sectional density profile with a thickness δ of 0.51 cm, chosen to match the diffusion thickness seen in the experiment. The domain is 16.7 cm wide (and deep in 3D) and 66.8 cm tall. The simulation is initialized such that the post-shock interface is stationary, and the initial location of the interface is chosen such that the full height of the domain is filled by the spike/bubble structure at the latest time for the single-mode-only case. Periodic boundary conditions are used in the spanwise directions and outflow conditions are used in the flow direction. These cases are called SM, MM_2D, MM_3D, and MM_3D_small and are detailed in Table I.

The four simulations chosen for the present work each exemplify a different aspect of dimensionality and interface geometry; together they illustrate the importance of 3D effects on a 2D-dominated flow. The SM simulation serves as a base case for the evolution of the dominant 2D wavenumber only. When compared to SM, the MM_2D case allows for the effects of small-scale perturbations in 2D to be explored. MM_3D brings the simulations into three dimensions, allowing for effects such as vortex stretching to impact the evolution of the RMI. Finally, MM_3D_small details the sensitivity of simulations to the small-scale 3D perturbations and visually best matches experimental images of the spike/bubble structure (see Fig. 2).

These simulations used the *Miranda* code, a high-order hydrodynamics code developed at Lawrence Livermore National Laboratory.¹⁷ This large eddy simulation code achieves high spatial accuracy using a 10th-order compact differencing scheme and is able to achieve high temporal accuracy by using a 4th-order accurate Runge-Kutta scheme. Energy is transported to sub-grid scales

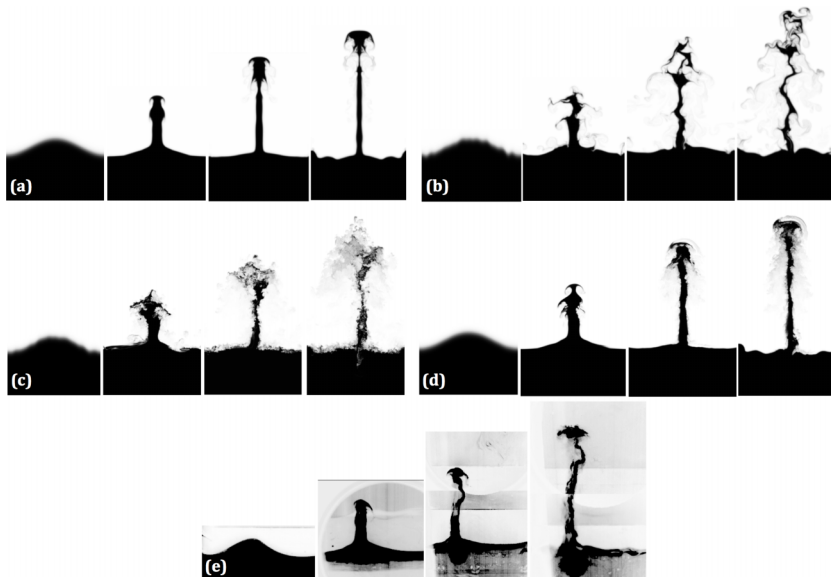


FIG. 2. Structure evolution shown at $\tau = 0$, $\tau = 3.62$, $\tau = 6.86$, and $\tau = 9.56$ for (a) single mode only (SM), (b) 2D single mode with $\frac{A_{rms}}{\eta} = 0.03$ multimode perturbations (MM_2D), (c) 3D single mode with $\frac{A_{rms}}{\eta} = 0.03$ multimode perturbations (MM_3D), (d) 3D single mode with $\frac{A_{rms}}{\eta} = 0.003$ multimode perturbations (MM_3D_small), and (e) experiment.¹⁶

through the use of artificial-fluid properties, such as hyper-viscosity and hyper-diffusivity. *Miranda* has proven useful in simulating a large variety of turbulent flows and mixing, including previous RTI and RMI studies.^{12,18}

III. RESULTS

A. Structure

Discussed here are the resulting structure and growth rate of the interface following acceleration by the shock wave, as well as mixing measurements for each case. As used previously in a number of RMI studies,^{16,19-21} both the interface amplitude and time will be nondimensionalized using Richtmyer's impulsive growth rate. The nondimensional amplitude is found by offsetting the measured height by the post-shock initial amplitude and then scaling by the single-mode wave number,

$$\bar{h} = k(h - h'_0), \quad (4)$$

where $k = \frac{2\pi}{\lambda}$ (with $\lambda = 16.7$ cm) is the dominant wavenumber, h is the measured height (at the 50% volume fraction level) for each time, and h'_0 is the post-shock initial amplitude. Here, $h'_0 = h_0 \left(1 - \frac{|V_0|}{Mc}\right)$, where h_0 is the initial amplitude, V_0 is the interface velocity jump, M is the Mach number, and c is the speed of sound in the light fluid. The nondimensional time τ is given by

$$\tau = kh'_0 t, \quad (5)$$

where t is the dimensional time and $h'_0 = kh'_0 A' V_0$ is the initial growth rate.

Figures 2(a)–2(d) show slices of volume fraction for each of the cases in Table I at $\tau = 0, 3.62, 6.86,$ and 9.56 after shock acceleration of the interface. This mimics what is seen experimentally using Mie scattering, shown in Fig. 2(e). In these images the dense SF₆ is black, the light He is white, and the shock direction is downward. All of these cases show the characteristic behavior of high Atwood number interface growth, where the dense upward-going spike becomes very narrow and the downward traveling bubble becomes very broad.

The evolution of the 2D single mode interface with no small-scale perturbations is shown in (a). When small-scale perturbations are added in 2D, as shown in (b), there is a clear break in the symmetry of the spike structure, and long, drawn-out, black and white filament structures are observed. When the domain is three-dimensional, shown in (c), the filament structures have broken into finer scale features and more mixing has occurred, as evident by the presence of more grey area. Finally, the 3D case with smaller multimode perturbations (case MM_3D_small) is shown in (d). In this case the spike structure is better preserved, and the mushroom-like structure at the tip of the spike remains intact but is surrounded by mixed material. The tip of the spike in the MM_3D case is more torn apart by the small-scale 3D features. The MM_3D_small case is the most visually similar to the experimental images shown in (e). At the latest time shown here, all cases show the bubble becoming distorted. This is also observed in the last experimental image.

Figure 3 shows each simulation case much later in time, at $\tau = 27$. In the 2D single mode case, Fig. 3(a), the spike has broadened, with secondary features spanning the width of the domain. A second harmonic becomes apparent at late times, with a spike developing at the original bubble location. At the later times of Fig. 2, the bubble has flattened and then experienced further instabilities from vorticity present in the light gas. By the latest time shown in Fig. 3, this motion on the bubble interface has caused light gas to be entrained below the interface. The MM_2D, Fig. 3(b), exhibits a similar vertical extent as the SM case, but the spike has mixed over a wider area without a coherent spike remaining and less concentrated heavy fluid. The base of the spike also exhibits a higher harmonic, but it appears shifted by a quarter wavelength. The 3D case, Fig. 3(c), in contrast to the 2D case, retains the coherent spike structure, although it has reduced in volume fraction compared to the single mode case. The vertical extent of the spike is reduced compared to the two 2D cases. A small downward-going jet of light material is extending beyond the base of the bubble. While a similar feature is visible in 2D, its extent is increased in 3D. When the amplitude of the multimode perturbations are decreased, as in Fig. 3(d), the overall extent approaches that of the 2D

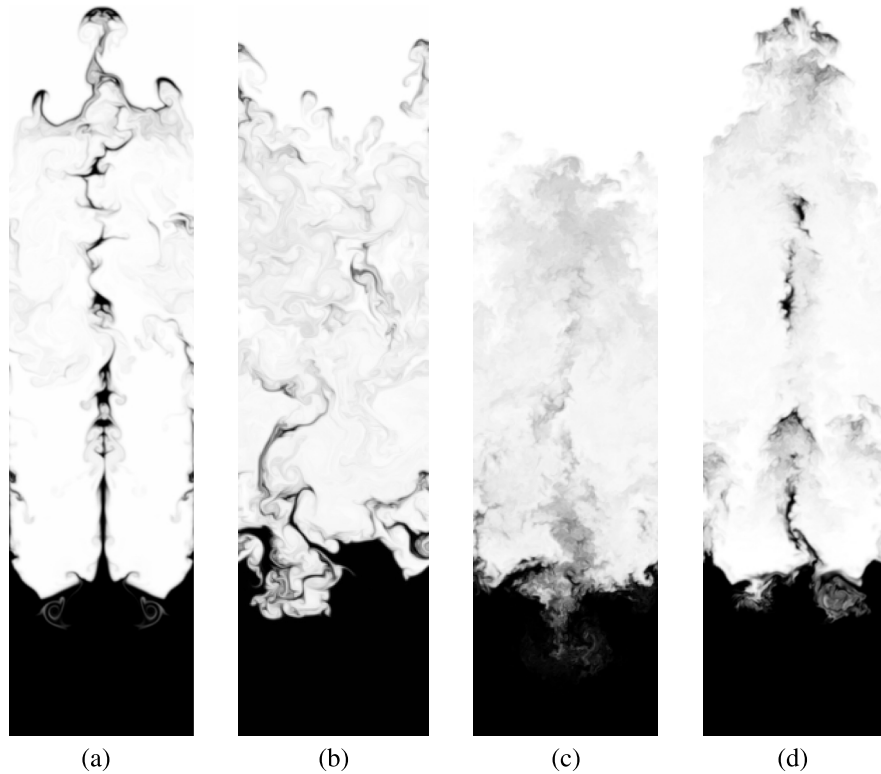


FIG. 3. Structure evolution shown at final time of $\tau = 27$ for (a) SM case, (b) MM_2D case, (c) MM_3D case, and (d) MM_3D_small case.

single mode case, but the spike appears broken at several locations, with clumps of little heavy gas remaining.

In the MM_3D case, a small downward jet of helium protrudes directly below the main spike. This can be observed in the latest time of Fig. 2(c) and in Fig. 3(c). In all simulations, a downward plume of material appears below the spike due the spanwise contraction of the spike (visible in images of the velocity field, shown in Fig. 4), but only in the MM_3D case is helium present in this plume. This plume is visible in the later-time experimental images of Fig. 2(e), but the experiments do not reveal if there is any helium contained in this plume. The presence of He in this plume in the simulation of case MM_3D appears to originate from the 3D effects, described in Fig. 5. This figure shows the interface viewed from below by showing the volume of $0.05 \leq \xi \leq 0.95$, where ξ

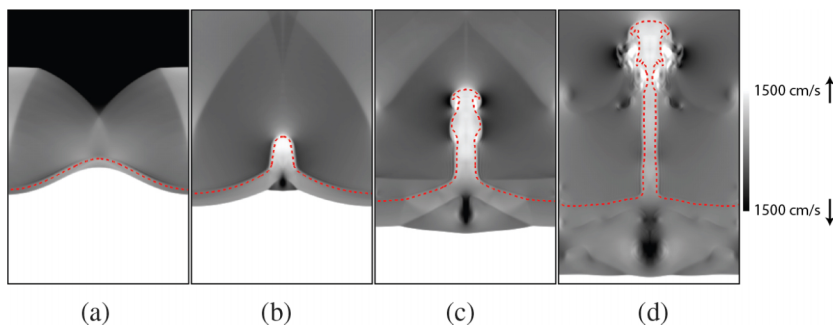


FIG. 4. Evolution of streamwise velocity showing the development of the upward-traveling interface spike, and the downward plume directly below the spike. The times are (a) $\tau = 0.54$, (b) $\tau = 1.62$, (c) $\tau = 3.62$, and (d) $\tau = 6.86$. The red dashed line shows the 50% volume fraction contour.

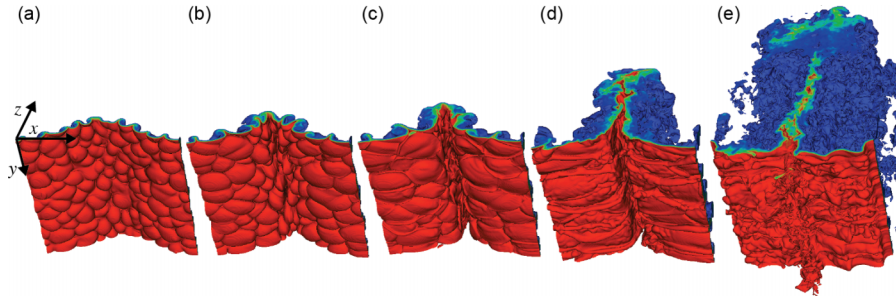


FIG. 5. Evolution of the interface in the MM_3D case. The material between $0.05 \leq \xi \leq 0.95$ is shown, viewed from the heavy material side. The multimode perturbations stretch in the x -direction and inject material downwards by the latest time. The times are (a) $\tau = 0.54$, (b) $\tau = 1.08$, (c) $\tau = 1.62$, (d) $\tau = 4.32$, and (e) $\tau = 10.8$.

is the volume fraction. The isotropically distributed 3D perturbations that are noticeable in (a) begin stretching in the x -direction as the spike contracts spanwise and grows in amplitude. The vortices pointed in the x -direction amplify in intensity during this three-dimensional process. By the time of (d) the bubble region of the interface contains narrow, downward-moving features that collide in the center and send a jet further downward, seen in (e).

B. Interface growth

While small-scale perturbations and three-dimensional effects visually change the interface, their effect on the interface height is small at early times. Fig. 6 shows the spike-to-bubble height for each simulation compared to experimental values, as well as growth rates for each case. In these figures, a red line denotes a 2D simulation and black lines show 3D cases. The solid lines represent cases with the same multimode amplitude (MM_2D and MM_3D cases). The red dotted line shows the SM case and the black dotted line shows the MM_3D_small case. For the 3D cases, 64 slices were used at various depths to find an average height value, modeling the data that might be obtained experimentally through an ensemble average. Figure 6(a) shows the development of the spike height, h , in time through measurements at the $\xi = 0.5$ contour level. At times earlier than $\tau \approx 2$, spike height is similar not only for all computational cases but also for experimentally determined values of h . While simulation appears to slightly over-predict h from $\tau \approx 2$ to $\tau \approx 6$, the MM_3D case agrees well with the experiment following $\tau \approx 6$, at which time this case and the other simulation begin to diverge with a deceleration in spike growth (see Fig. 6(b)). This transition to nonlinear growth is later followed by the MM_2D case at $\tau \approx 16$, while the single mode and small A_{RMS} cases continue on at roughly 8 cm/ms. Previous work¹⁹ found 2D simulations to over-predict

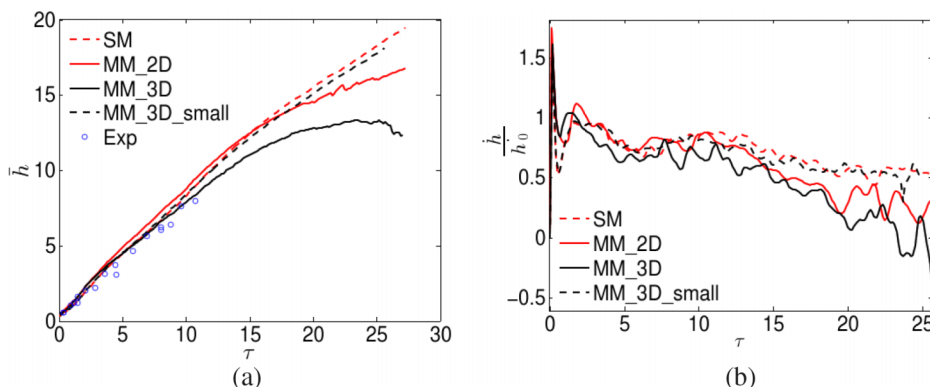


FIG. 6. Spike-to-bubble extent as defined by the $\xi = 0.5$ contour level, (a) height and (b) growth rate in time. Open circles in (a) show experimental values from Motl *et al.*¹⁶

the experimental interface height, which also seems to be occurring here in all but the case with larger multimode perturbations, although the difference found here is small.

Growth rates show (Fig. 6(b)) that, compared to the single mode only case, there is a small increase in growth at early times from adding small-scale perturbations in 2D and 3D, but this reduces to a negligible difference in the MM_3D_small case. Following this initial peak in growth rates, all cases show a relatively constant decay in growth until $\tau \approx 6$. At this time, the growth rate for the MM_3D case begins to decay at a higher rate than the others. Later, a similar decay is seen for the MM_2D case beginning at $\tau \approx 14$. The MM_3D_small case only has a slight reduction in growth rate compared to the SM case. The growth rate from the MM_3D case actually becomes negative after $\tau \approx 22$. This is because the increased molecular mixing in 3D reduces the concentration of spike material to where the extent of the $\xi = 0.5$ contour begins decreasing.

C. Mixing

The integral mixing width takes into account the volume fraction over the entire domain to obtain a width and does not suffer from contour thresholds like the definition for h . This integral is readily available from the simulations but difficult to measure in experiments; therefore, only the simulation values are shown here. The integral mixing width²² is described by

$$W = \int_{-\infty}^{\infty} \bar{\xi}(1 - \bar{\xi}) dz, \quad (6)$$

where the average volume fraction is given by

$$\bar{\xi} = \begin{cases} \frac{1}{L_x} \int_0^{L_x} \xi dx & \text{for } 2d \\ \frac{1}{L_x L_y} \int_0^{L_y} \int_0^{L_x} \xi dx dy & \text{for } 3d \end{cases}, \quad (7)$$

where L_x is the width of the domain and L_y is the depth of the domain.

The integral mixing width is nondimensionalized using the dominant wavenumber, k , and shown in Fig. 7. There appears to be three epochs occurring. Before $\tau = 3.8$, the mixing width is growing linearly and with general agreement among all cases. From $\tau = 3.8$ to $\tau = 9.2$, W does not increase in the SM case. From the previous figure, we know that the height of the interface is still growing, so it appears that the increase in height is offset by the average volume fraction, $\bar{\xi}$ becoming closer to 0 or 1 (depending on the definition of ξ). In the other cases, mixing caused by small-scale perturbations is pushing $\bar{\xi}$ towards 0.5 and thereby increasing W . During this second epoch, the increased mixing produced by 3D effects causes the 2D and 3D cases with the same A_{RMS} to separate (solid lines). In the final epoch, the spike breaks apart and increases the amount of

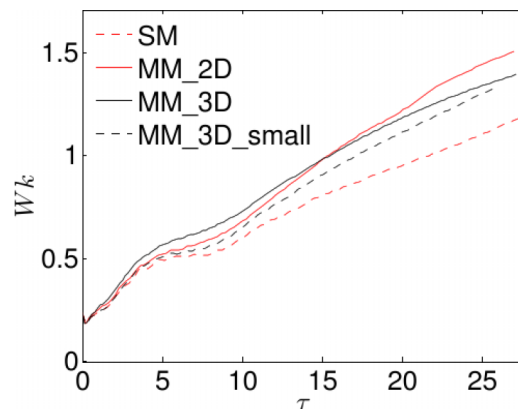


FIG. 7. Integral mixing width, Eq. (6), for the four simulation cases.

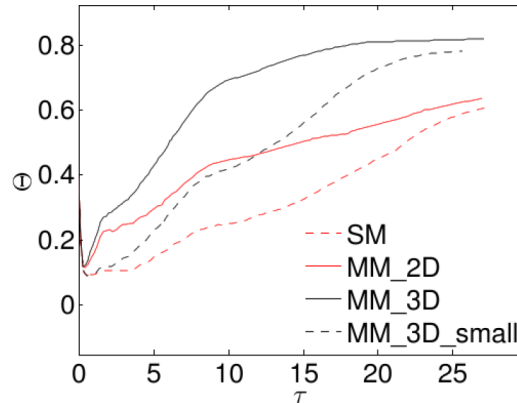


FIG. 8. Mixedness ratio, Eq. (8), for the four simulation cases.

mixing and the mixing width. Three-dimensional effects are observed during this final period as the MM_2D case grows faster than the MM_3D case. Additionally, the MM_3D_small case is growing faster than the SM case at later times.

The relative amount of molecular mixing can be computed through the mixedness ratio,

$$\Theta = W^{-1} \int_{-\infty}^{\infty} \overline{\xi(1-\xi)} dz. \quad (8)$$

Mixedness is a measure of the amount of mixing occurring within the mixing width, with 0 being unmixed and 1 being completely mixed. The mixedness for each case is shown in Fig. 8. While Θ may not be converged for a very-high Reynolds number flow, comparing simulations with the same resolution (and therefore the same numerical Reynolds number) illustrates how the dynamics change from 2D to 3D and with varied amounts of 3D perturbations. Additionally, work by Olson and Greenough¹³ shows Θ to approach a converged value at the resolution used in this study. In all cases, the mixedness decreases immediately following the passage of the shock wave due to the compression of the interface and early linear growth. After this initial decrease in Θ , the mixedness increases monotonically for all simulations. This increase happens slowly for the SM and MM_3D_small cases and rapidly for the MM_2D and MM_3D cases. Regardless of a slow or rapid initial increase in mixedness, Fig. 8 clearly shows that the most important factor in determining a simulation's mixedness at late-time is the dimension in which the simulation is run. By the latest time, an obvious separation is seen in the value of mixedness for 2D and 3D simulations despite delayed mixing in the small A_{RMS} and single mode cases. In the present study, two-dimensional cases are converging toward a mixedness value that is only about 75% that of the three-dimensional cases.

IV. CONCLUSIONS

This study has shown that 3D effects are important in completely understanding the development of the RMI, even when the flow is dominated by 2D features. The 3D simulation with small-scale multimode perturbations of $A_{RMS}/\eta = 0.003$ shows good visual agreement with the experimental images. At this small level of multimode perturbations, the interface height is not significantly altered from the single mode case. With larger amplitude multimode perturbations, 2D and 3D simulations show a divergence in interface height. The integral mixing width depends on both the dimensionality of the simulation and the presence of small scale perturbations. 3D effects have also been found to have a different effect on spike/bubble height and integral mixing width. Although perturbations and three-dimensionality work to reduce h at late times, we find that W is largest for these cases when compared with the single-mode-only case.

The amount of mixing occurring directly after shock-acceleration is strongly dependent on small-scale features and is increased by 3D effects. At the latest-time however, results show

that the value of mixedness appears to only depend on the dimension in which the simulation was computed, with 2D and 3D results converging to different values. This implies that a two-dimensional domain will not be able to accurately represent all aspects of the RMI since, at a minimum, the level of mixing will be under-predicted.

ACKNOWLEDGMENTS

Part of this work was performed under the auspices of the U.S. Department of Energy by Lawrence Livermore National Laboratory under Contract No. DE-AC52-07NA27344. A portion of this research was supported by DOE Grant No. DE-NA0001980. The authors are grateful for the support of the WCI HEDP summer program at LLNL and the assistance of A. Cook and W. Cabot.

- ¹ Lord Rayleigh, "Investigation of the character of the equilibrium of an incompressible heavy fluid of variable density," *Proc. London Math. Soc.* **14**(1), 170–177 (1883).
- ² G. Taylor, "The instability of liquid surfaces when accelerated in a direction perpendicular to their planes. I," *Proc. R. Soc. A* **201**(1065), 192–196 (1950).
- ³ R. D. Richtmyer, "Taylor instability in shock acceleration of compressible fluids," *Commun. Pure Appl. Math.* **13**(2), 297–319 (1960).
- ⁴ E. E. Meshkov, "Instability of a shock wave accelerated interface between two gases," NASA Tech. Transl. **13**, 1–14 (1970).
- ⁵ D. J. Acheson, *Elementary Fluid Dynamics* (Clarendon Press, Oxford, 1990).
- ⁶ H. Tennekes and J. L. Lumley, *A First Course in Turbulence* (The MIT Press, 1972).
- ⁷ B. J. Balakumar, G. C. Orlicz, C. D. Tomkins, and K. P. Prestridge, "Simultaneous particle-image velocimetry–planar laser-induced fluorescence measurements of Richtmyer-Meshkov instability growth in a gas curtain with and without reshock," *Phys. Fluids* **20**(12), 124103 (2008).
- ⁸ A. A. Gowardhan and F. F. Grinstein, "Numerical simulation of Richtmyer-Meshkov instabilities in shocked gas curtains," *J. Turbul.* **12**, N43 (2011).
- ⁹ O. Schilling and M. Latini, "High-order WENO simulations of three-dimensional reshocked Richtmyer-Meshkov instability to late times: Dynamics, dependence on initial conditions, and comparisons to experimental data," *Acta Math. Sci.* **30**, 595–620 (2010).
- ¹⁰ M. Vetter and B. Sturtevant, "Experiments on the Richtmyer-Meshkov instability of an air/SF₆ interface," *Shock Waves* **4**, 247–252 (1995).
- ¹¹ W. Cabot, "Comparison of two- and three-dimensional simulations of miscible Rayleigh-Taylor instability," *Phys. Fluids* **18**, 045101 (2006).
- ¹² W. H. Cabot and A. W. Cook, "Reynolds number effects on Rayleigh–Taylor instability with possible implications for type Ia supernovae," *Nat. Phys.* **2**(8), 562–568 (2006).
- ¹³ B. J. Olson and J. Greenough, "Large eddy simulation requirements for the Richtmyer-Meshkov instability," *Phys. Fluids* **26**, 044103 (2014).
- ¹⁴ V. A. Smalyuk *et al.*, "Hydrodynamic instability growth and mix experiments at the National Ignition Facility," *Phys. Plasmas* **21**(5), 056301 (2014).
- ¹⁵ V. A. Smalyuk *et al.*, "First measurements of hydrodynamic instability growth in indirectly driven implosions at ignition-relevant conditions on the National Ignition Facility," *Phys. Rev. Lett.* **112**(18), 185003 (2014).
- ¹⁶ B. Motl, J. Oakley, D. Ranjan, C. Weber, M. Anderson, and R. Bonazza, "Experimental validation of a Richtmyer-Meshkov scaling law over large density ratio and shock strength ranges," *Phys. Fluids* **21**(12), 126102 (2009).
- ¹⁷ A. W. Cook, "Artificial fluid properties for large-eddy simulation of compressible turbulent mixing," *Phys. Fluids* **19**(5), 055103 (2007).
- ¹⁸ C. R. Weber, A. W. Cook, and R. Bonazza, "Growth rate of a shocked mixing layer with known initial perturbations," *J. Fluid Mech.* **725**, 372–401 (2013).
- ¹⁹ C. Weber, B. Motl, J. Oakley, M. Anderson, and R. Bonazza, "Richtmyer–Meshkov parameter study," *Fusion Sci. Technol.* **56**(1), 460–464 (2009).
- ²⁰ J. Jacobs and V. Krivets, "Experiments on the late-time development of single-mode Richtmyer-Meshkov instability," *Phys. Fluids* **17**, 034105 (2005).
- ²¹ O. Sadot, L. Erez, U. Alon, D. Oron, L. Levin, G. Erez, G. Ben-Dor, and D. Shvarts, "Study of nonlinear evolution of single-mode and two-bubble interaction under Richtmyer-Meshkov instability," *Phys. Rev. Lett.* **80**, 1654 (1998).
- ²² D. L. Youngs, "Numerical simulations of mixing by Rayleigh-Taylor and Richtmyer-Meshkov instabilities," *Laser Part. Beams* **12**, 725 (1994).